Journal of Solar Energy Research (JSER)

Journal homepage: www.jser.ut.ac.ir

Enhancing the Performance of a Double-Slope Solar Still Using Hollow Fins and Porous Sponge: A Numerical Study

Omer Rafee Shehadeh[a*], Fadhil Abdulrazaq Kareem[b], Hayder M. B. Obaida[a,]

[a]*Engineering Technical College, Baghdad, Middle Technical University, Baghdad, Iraq*
[b]*Power Mechanics Techniques, Polytechnic College of Engineering, Specialization, Baghdad, Middle Technical University, Baghdad, Iraq*

ARTICLE INFO

Article Type:

Research Article

Received:2026.07.22
Accepted in revised form:2026.10.30

Keywords:
Double-slope solar still; Hollow fins; Porous sponge; Capillary effect; ANSYS; Thermal efficiency

A B S T R A C T

Low productivity is a big problem in the conventional solar stills. A double-slope solar still (DSSS) with hollow cylindrical fins (HCF) and porous sponges (PS) has been numerically analyzed in this study for optimum performance in the climatic conditions of Baghdad, Iraq. A parametric study was performed using ANSYS Fluent to assess glass inclination, hollow fin configuration and porous sponge structure. The ideal inclination angle is found to be 32° so that maximum amount of solar energy is absorbed and condensed. The water productivity of hollow fins is improved from 2.93 to 5.03 kg/m2-day by incorporating hollow fins. The use of porous sponges enhances the capillary driven thin film evaporation further. The best arrangement is segmented square sponge arrangement with 42 hollow fins where a maximum fresh water production of 8.79 kg/m2·day and thermal efficiency of 38.8% are obtained. This hybrid integration is an effective, economical and passive approach to upgrade solar desalination. The system enhances the productivity of the freshwater by 200% of its baseline productivity making it a highly viable sustainable solution to water generation in dry areas.

1. Introduction

Over the last 100 years, freshwater has been consumed on a large scale worldwide. [1]. Although approximately 70% of the Earth's surface is covered by water, nearly 97% of this water is saline, with only 3 % being fresh water, the majority of which is contained in ice and ground water, meaning that only

*Corresponding Author Email: abc5007@mtu.edu.iq

Cite this article: Rafee Shehadeh, O., Kareem, F. Abdulrazaq & Obaida, H. Mahde. (2026). Enhancing the Performance of a Double-Slope Solar Still Using Hollow Fins and Porous Sponge: A Numerical Study. Journal of Solar Energy Research, 11(4), 3384–3402. https://doi.org/10.22059/jser.2026.419084.1772

DOI: 10.22059/jser.2026.419084.1772

©The Author(s). Publisher: University of Tehran Press.

a small percentage of water is easily available to man, as indicated in Figure 1 [2]. This limited availability highlights the growing global challenge of freshwater scarcity. To address this challenge, desalination has emerged as an effective means of turning saline water into drinking water. [3]. Nevertheless, traditional desalination methods tend to be energy-consuming and very expensive. Thus, as an alternative, low-cost, sustainable solution, solar-driven desalination systems have attracted increasing interest, especially in areas with high levels of solar radiation. Among these systems, the double-slope solar still (DSSS) demonstrates superior performance compared to conventional designs. It uses two sloping glass covers that help boost solar energy uptake and increase the size of the condensation area. Within this mechanism, the solar radiation warms saline water, causing evaporation, and subsequent condensation onto the glass surfaces to make fresh water [4].

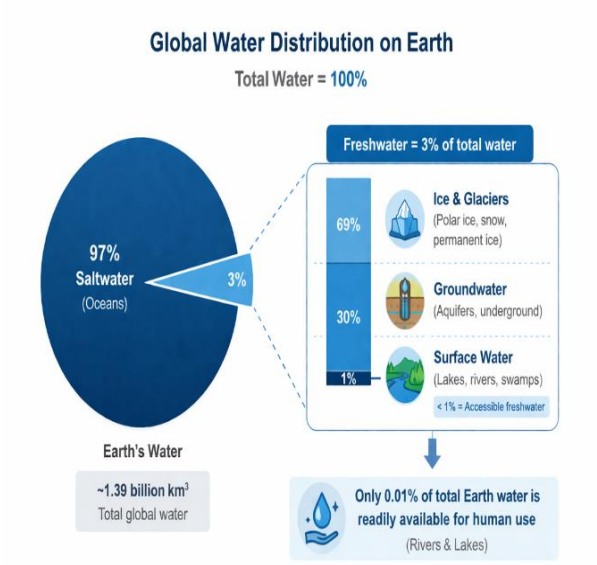


Figure 1. Global distribution of water on Earth. Data based on USGS & UNESCO estimates

Rajaseenivasan et al. [5] examined the theoretical and experimental performance of a single slope solar still (SSSS) by adding circular and square fins, some of which were covered with wick material. This study was conducted in Madurai, Tamil Nadu, India (9°56′N, 78°07′E) with water depths ranging from 1 to 4 cm. The highest daily productivity was recorded with square fins equipped with a wick, at 4.55 L/m²·day, and the highest productivity rate was 45.8% compared to the traditional solar still. Khare et al. [6] developed a computational fluid dynamics (CFD) model for the SSSS in Jaipur, India (26°13'N, 75°49'E). The model was conducted at varying depths and with different black materials to determine the highest productivity using the ANSYS program under prevailing climate conditions. The simulation results demonstrated that the highest productivity was 5 L/m²·day, the maximum efficiency of the solar system was 32%, and the highest productivity ratio with mirrors was approximately 22% compared to a traditional system. Moreno et al. [7] conducted a study analysing the effect of energy storage by adding a phase change material (PCM) to the base of an SSSS. They reported a relative difference of less than 1%. The CFD simulation system was situated in Hermosillo, Sonora, Mexico (29°05′N, 110°57′W) during the winter and summer. A desert climate characterizes the city of Hermosillo. Four different materials were utilized to analyse the effect of adding PCM at different phase-change temperatures and latent heats, using several types of PCM (RT70 HC, RT54 HC, RT62 HC, RT80 HC) and thicknesses of 0.25, 0.5, and 1 cm. The highest productivity was observed at 0.25 cm and RT70 HC, at approximately 5.42 L/m²·day, and the highest efficiency was approximately 66.70% compared to a traditional solar still. Hafs et al. [8] conducted a study in Rabat, Morocco (34°02′N, 6°50′W) to demonstrate the seasonal thermal performance in SSSS. The study used rectangular channels filled with heat-storage materials. It employed the finite element method in COMSOL Multiphysics to predict the effects of various engineering design parameters, including the Number and width of the rectangular channels. The study then selected the optimal configuration for several different seasons to achieve the highest productivity. The highest productivity, 2.92 L/m²·day, and an overall thermal efficiency of 157% were observed in summer when using five rectangular channels, each 2 cm wide. Hameed et al. [9]conducted a study using COMSOL to demonstrate an increase in the evaporation area. A three-dimensional model of the system was prepared by adding 15 stainless steel to the system basin in different configurations. In Najaf, Iraq (32.0316°N, 44.3219°E), the highest productivity was 4.13 L/m²·day, and the maximum temperature was 72.9 °. Aftiss et al. [10] conducted a numerical comparison of an SSSS in six regions of Morocco for each season of the year. In the initial case, paraffin wax was utilized as a phase change material (PCM), while in the subsequent case, it was connected to a storage tank. The findings were then compared with experimental data, and it was observed that the highest productivity was recorded in Cass two in Marrakesh (31.6295°N, 7.9811°W) at 8.6 L/m² ·day.

In contrast, the highest energy efficiency was achieved in Agadir (30.4278°N, 9.5981°W) at 76.05%. Abdulmajid et al. [11] conducted a study that examined the effect of the optical properties of the glass cover on SSSS solar desalination systems. The study tested the transmittance, absorptance, and reflectance of the glass cover under various operating conditions in Matruh, Egypt (31.35°N, 27.25°E) to improve productivity and efficiency in the desalination process. The results showed that as the glass thickness increased from 5 to 20 mm, daily productivity and efficiency decreased from 6.6 to 5.2 L/m²·day and from 31.5% to 24.9%, respectively. The highest productivity was achieved when using glass with optimal optical properties, such as low refractive index and low absorption coefficient, and a smaller thickness, with an optimal monthly variable angle of inclination. This resulted in a maximum productivity of 210 L/m²·summer month and daily efficiency of 36%. In the summer, glass types such as Pyrex or quartz, which increase light transmission and reduce reflection, should be used, with the angle of inclination adjusted monthly to suit the location. Abed et al. [12] conducted a numerical simulation study using the COMSOL Multiphysics program under climatic conditions in Najaf, Iraq (32.0316°N, 44.3219°E) for a pyramid solar still (PSS). The maximum productivity achieved was 8.14 L/m²/day, and a 112.34% improvement in daily energy efficiency was observed when using flat reflectors, PCM, and CuO nanoparticles**.** Aftiss et al. [13] conducted a numerical study on a sunny day in the city of Agadir, Morocco (30.4278°N, 9.5981°W) to improve the efficiency of SSSS by applying a dynamic layer of phase-change material PCM. The results showed that the highest productivity reached 6.04 L/m²·day, and energy efficiency was 62.11%. The maximum freshwater production was increased by around 23.26%. While there is significant work in the realm of improving solar still performance, most studies treat single modification techniques (such as extended surfaces, or porous media), and very little research has focused on the synergistic effects of these combined. This work fills this gap by presenting three novelties in the field of solar desalination. Its main contribution is a novel combined passive enhancement approach, which combines the combination of hollow fins and segmented porous sponges in a Double-Slope Solar Still (DSSS) design. The unique combination of this heat transfer area is maximized, and the capillary action of the sponge provides a continuous thin-film evaporation. Second, it adopts a complete computational fluid dynamics (CFD) modelling method to explicitly capture the thermo-capillary coupling interaction between these components, showing a critical shift from the thermal-limited to mass-transfer-limited evaporation in the still. Lastly, this hybrid system is tested under the extreme arid climatic conditions in Baghdad, Iraq, which is highly realistic and gives a realistic estimation of its viability under climatic conditions where there is high solar radiation and very limited water availability, where elevated solar irradiance and ambient temperature markedly affect system performance. Consequently, a clear gap exists in formulating and evaluating a hybrid passive enhancement strategy that simultaneously improves heat transfer, water distribution, and evaporation efficiency in DSSS systems. The current study seeks to fill this gap by presenting an innovative configuration that combines hollow fins with both continuous and segmented porous sponge structures, and by conducting an extensive CFD-based examination of the fundamental physical mechanisms and their influence on freshwater productivity.

2. Physical Description Model

2.1. The inclination angle model being investigated

It was chosen that the water house of Double-Slope Solar Still (DSSS) is pitched-roof (gable) in shape to enable the maximum utilization of solar energy during the day and also to give quite a considerable amount of condensation area as compared to the conventional type of single-slope Solar Still. The orientation of the longitudinal axis of the DSSS is along North-South to maximise solar interception with the two sloped glass covers oriented towards East and West to capture the morning and afternoon solar radiation. Case I was investigated regarding the geometrical parameters of the still and the effect of changing the geometrical parameters of the DSSS by changing the inclination angles and wall heights as shown in Table 1. The latitude of Baghdad, Iraq (33.3152° N, 44.3661° E) was put into the model ANSYS simulation. using a constant basin length of 1000 mm, a width of 1000 mm, and a partial height of 100 mm. The anchored pleat length was set at 1000 mm, and the thickness was 1 mm, as seen in Figure 2.

Table 1. various geometrical dimensions of the angles DSSS

Angle °	heights of wall mm	Chord Length mm
23	330.5314	550.5858029
24	339.9746	554.6059941
25	349.3448	558.7242874

26	358.639	562.9335061
27	367.8544	567.2265681
28	376.9882	571.5964161
29	386.0377	576.0360803
30	395	580.5385431
31	403.8725	585.0969973
32	412.6524	589.7046068
33	421.337	594.3546648

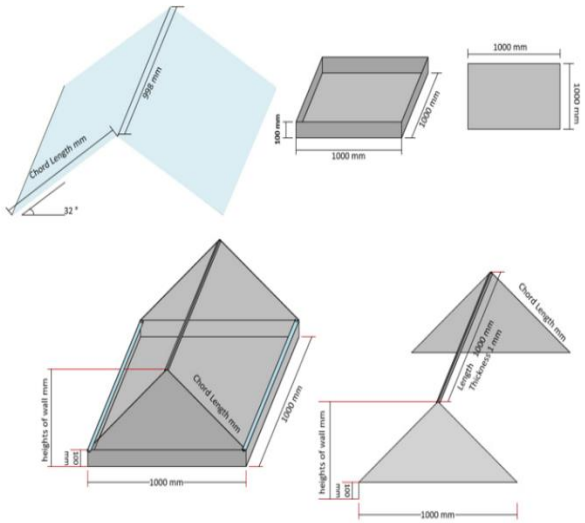
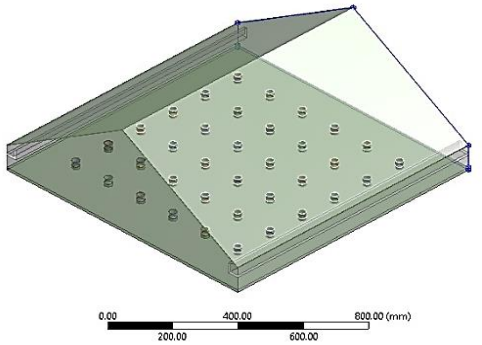


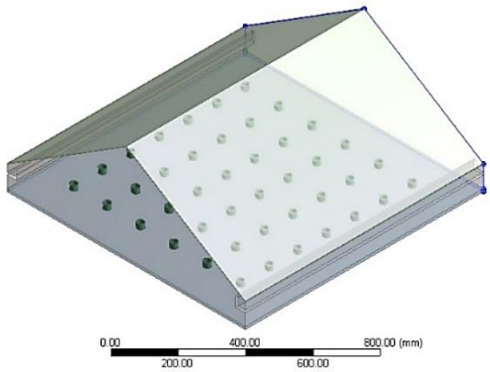
Figure 2. Schematic diagram and geometric dimensions of the DSSS

2.2. The hollow fins model being investigated

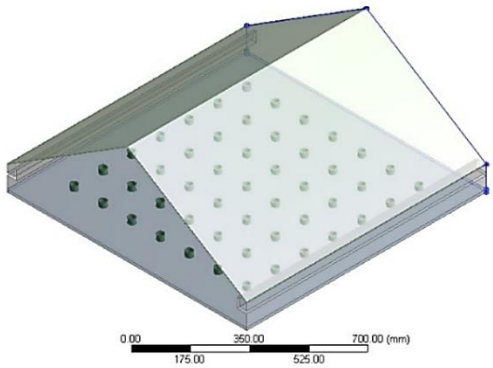
Three models of hollow fins were simulated in this investigation with a 3 cm fin height, 26.5 mm outer and 24.5 mm inner diameter, as shown in Figure 3. These models were designed using the best dimensions obtained in Case I of the DSSS. Case II had 36 fins, Case III had 42 fins, and Case IV had 49 fins. These fin counts were chosen, because they make sense in terms of geometric arrays, which would be 6x6, 7x7 and a staggered 6x7 for example, as well as a 6x6 intermediate stagger, and which fit uniformly into the 1000 mm x 1000 mm absorber basin. A uniform arrangement was strictly observed with a progressive increase in the effective heat transfer area while maintaining sufficient spacing between the hollow fins. This critical spacing is important to avoid thermal interference from adjacent fins, and to allow for a free-flowing natural convection process in the fluid domain.



Case II: Model of 36 fins



Case III: Model of 42 fins



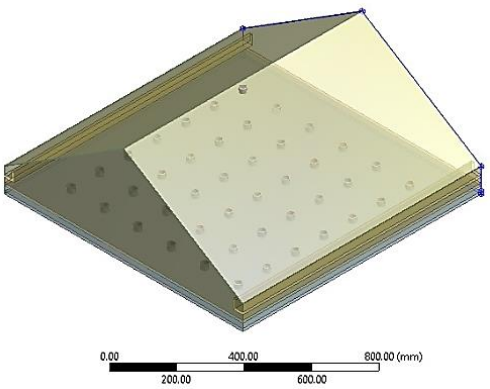
Case IV: Model of 49 fins

Figure 3. Fin model configurations in a DSSS (Case II, III, and IV)

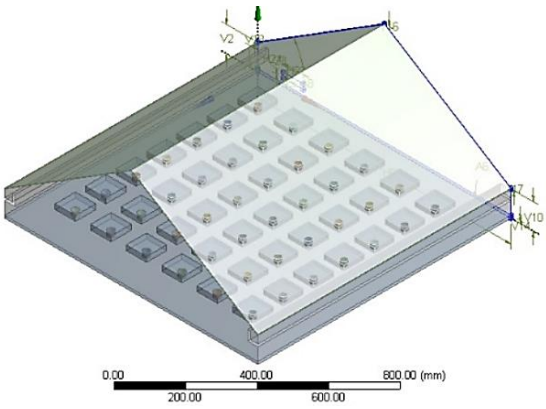
2.3. The hollow fins with sponge model being investigated

Two distinct strategies were employed based on the hybrid integration of hollow fins and structured porous sponges within the solar thermal system.

The similar-performing dimensions (42-fin) were used in both models, as shown in Figure 4. In the first strategy, a 3-cm-height sponge layer, 1-cm-thick, and 1000 x 1000 mm in size was placed on top of the fins, which represents case V. In the case VI (second strategy), the square sponge was placed on top of each fin, which had dimensions 80 mm x 20 mm. all cases summarized in table 2.



Case V: 42 fins with sponge



Case V: 42 fins with black square sponge

Figure 4. Models of a sponge on hollow fins

Table 2. Case designations used in the study

Case	Description
Case I	Conventional DSSS without modifications
Case II	DSSS with 36 hollow fins
Case III	DSSS with 42 hollow fins
Case IV	DSSS with 49 hollow fins
Case V	DSSS with 42 hollow fins + continuous porous sponge layer
Case VI	DSSS with 42 hollow fins + square porous sponge pieces

3. Mathematical Model

3.1 Governing equations

Continuity equation: mass conservation in fluid flow, as shown in equation (1), Navier–Stokes equation: describing the motion of viscous fluids under the influence of pressure, viscosity, and external forces, as shown in equation (2), Energy equation: describing heat transfer in fluids with the effects of thermal conduction and internal sources, as shown in equation (3), and viscous dissipation: thermal energy generated by internal friction in fluids, as shown in equation (4) [14, 15].

$$\rho \nabla . \vec{v} = 0 \tag{1}$$

$$\left(\vec{v}.\nabla\vec{v}\right) = -\frac{\nabla P}{\rho} + \nu\nabla^2\vec{v} + \vec{f} \tag{2}$$

$$\rho C_p\left(\left(\vec{v}.\nabla\right)T\right) = K\nabla^2 T + \phi \tag{3}$$

$$\phi = \mu\left\{\begin{array}{l} 2\left[\left(\frac{\partial u}{\partial x}\right)^2 + \left(\frac{\partial v}{\partial y}\right)^2 + \right. \\ \left.\left(\frac{\partial w}{\partial z}\right)^2\right] + \left(\frac{\partial v}{\partial x} + \frac{\partial u}{\partial y}\right)^2 + \\ \left(\frac{\partial w}{\partial y} + \frac{\partial v}{\partial z}\right)^2 + \left(\frac{\partial u}{\partial z} + \frac{\partial w}{\partial x}\right)^2 \end{array}\right\} \tag{4}$$

3.2 Heat Transfer between Water and the Condensing Glass Cover by Convection

The concentration of water vapor within the solar still varies, providing a buoyancy force that promotes convective heat transfer. The convective movement of heat between the saline water surface and the condensing glass cover Q_{Cw} [W/m^2] is indicated by [16]:

$$Q_{Cw} = h_{Cw} \times A_W \times \left(T_W - T_g\right) = h_{Cw} \times A_W \times \Delta T \tag{5}$$

where h_{Cw} represents the convective heat transfer coefficient [W/m^2.℃], Aw represents the area of the water surface [m^2], ΔT is the temperature difference. The coefficient h_{Cw} is determined as the result of fluid properties, operating temperatures, still geometry, and flow conditions. It has a relation with the Nusselt number (Nu) [17]:

$$Nu = \frac{\left(h_{Cw} \times d\right)}{K} = C \times \left(Gr \times Pr\right)^n \tag{6}$$

d: The characteristic length of the still (approach to mean distance between water surface and glass) and (W/m·K): thermal conductivity of water vapor. Pr

and Gr are the Prandtl and Grashof numbers (dimensionless), and n and C are linear regression constants. The convective heat transfer coefficient h_{Cw} can be calculated as follows [18]:

$$h_{Cw} = \frac{(C \times K)}{d}(Gr \times Pr)^n \quad (7)$$

Grashof and Prandtl numbers may be formulated in the following form [18]:

$$Gr = \frac{\left(g \times \beta \times d^3 \times {\rho_v}^2 \times \Delta T\right)}{\mu^2} \quad (8)$$

where g is the acceleration due to gravity (9.807 m/s²), β is the coefficient of volumetric thermal expansion (K^{-1}), ρ_v is the density of the water vapor in the solar still (kg/m³), ΔT is the temperature difference between the water surface and the glass lid (°C), and μ is the dynamic viscosity of the water vapor in the solar still (N·s/m²) [18].

$$Pr = \frac{\mu \times C_v}{K} \quad (9)$$

C_v is the specific heat capacity of the water vapor (J/kg·°C). As reported in [18] The thermo-physical characteristics of water vapor that are temperature-dependent were obtained and could be represented as follows:

$$K = 0.0244 + 0.7673 \times 10^{-4} \times T_g \quad (10)$$

$$\rho_v = \frac{353.44}{(T_v + 273.15)} \quad (11)$$

$$\beta = \frac{1}{(T_v + 273.15)} \quad (12)$$

$$\mu = 1.718 \times 10^{-5} + 4.620 \times 10^{-8} \times T_v \quad (13)$$

$$C_v = 0.1434 \times T_v + 1.101 \times 10^{-4} \times T_v - 6.7581 \times 10^{-8} \times {T_v}^3 + 999.2 \quad (14)$$

$$h_{fg} = 2.4935 \times 10^6 \left(\begin{array}{l} 1 - 9.4779 \times 10^{-4}\ T_v + \\ 1.3132 \times 10^{-7}\ T_v^2 - \\ 4.7974 \times 10^{-9}\ T_v^3 \end{array}\right) \quad (15)$$

The convective heat transfer coefficient, $h_{cw,D}$[W/m²·°C] between the water surface and the condensing glass cover of the still can be expressed as follows [19]:

$$h_{cw,D} = 0.884 \times \left[\begin{array}{l} (T_w - T_g) + \\ \dfrac{(P_w - P_g)}{268.9 \times 10^3 - P_w} \times \\ (T_w + 273.15) \end{array}\right]^{\frac{1}{3}} \quad (16)$$

The DSSS is working in the passive mode in the current research. In this regard, the convective heat transfer coefficient between the saline water and the condensing glass cover, as per the Clark model ($h_{cw,CL}$) is the same as that calculated using the Dunkle model. It is obtained from equation (16) [20]. Conversely, as per the Kumar and Tiwari model, the convective heat transfer coefficient ($h_{cw,KT}$) between saline water and the condensing cover is calculated with the help of the constants n and C whose values are 0.4114 and 0.0322, respectively, as stated in equation (7) [17].

3.3 Evaporative Heat Transfer to the Condensing Cover

To calculate the amount of distilled water, the following relation is used. [21]:

$$m_{ew} = \frac{q_{ew} \times A_W \times t_{int}}{h_{fg}} \quad (17)$$

Where $q_{ew} = h_{ew} \times (T_w - T_g)$ (18)

and $h_{ew} = 16.23 \times 10^{-3} \times h_{cw} \dfrac{(P_w - P_g)}{(T_w - T_g)}$ (19)

Where A_W is the surface area of the saline water (m²), t_{int} is the time interval (s) and $h_{fg}$is the latent heat of vaporization of water (J/kg). Dunkle model expression in [18] indicates that the coefficient of evaporative heat transfer, h_{ewD} (W/m²·°C) The amount of saline water to the condensing cover can be determined:

$$h_{ewD} = 16.23 \times 10^{-3} \times h_{cwD} \frac{(P_w - P_g)}{(T_w - T_g)} \quad (20)$$

The pressures P_w and P_g can be calculated according to the following formulae [22]:

$$P_w = e^{\left(\frac{25.317 - 5144}{T_w + 273.15}\right)} \quad (21)$$

$$P_g = e^{\left(\frac{25.317 - 5144}{T_g + 273.15}\right)} \quad (22)$$

Replacing equation (7) with equation (20): the evaporative heat transfer coefficient h_{ew} can be reworked as follows:

$$h_{ew} = 0.01623 \times \frac{K}{d} \times C \times (Gr \times Pr)^n \times \left[\frac{(P_w - P_g)}{(T_w - T_g)}\right] \quad (23)$$

The mass transfer rate m_{ew}, can be expressed as follows [18] when equation (17) is replaced with equation (18) and (23):

$$m_{ew} = \frac{0.01623}{\mathrm{h_{fg}}} \times \frac{K \times A_W \times t_{int} \times \mathrm{C}}{d} \times \left(P_w - P_g\right) \times \left(Gr \times Pr\right)^n \quad (24)$$

As this is a purely numerical study, there is no physical measurement of distilled water yield, but rather, the yield of distilled water is calculated numerically by integrating this mass transfer rate (m_{ew}) over the computed diurnal cycle, thus determining the total freshwater productivity (kg/m²·day). The hourly thermal efficiency can then be calculated as follows [23, 24].

The hourly thermal efficiency can be calculated as follows[23, 24]:

$$\eta_h = \frac{m_{ew} \times \mathrm{h_{fg}}}{I \times \tau.\alpha \times A_W \times 3600} \quad (25)$$

Where:

I: Global horizontal irradiation (W/m^2), and $\tau.\alpha$: transmittance − absorptance product, the numerical value of which is about 0.9[25]. To simulate fluid flow and heat transfer through the porous sponge structures (Cases V and VI), the ANSYS Fluent Porous Media model was utilized. Because the base of the sponge is continuously submerged in the saline water basin, the sponge matrix is assumed to be fully saturated ($s = 1.0$) via passive capillary wicking, maintaining a continuous thin liquid film at the upper evaporation interface. Macroscopic flow through the porous zone is governed by adding a momentum source term (S_i) to the standard Navier–Stokes equations (Darcy–Forchheimer law) [30, 32]:

$$S_i = -\left(\frac{\mu}{K} u_i + \frac{C_2}{2} \rho |u| u_i\right) \quad (26)$$

where K is the permeability of the porous sponge (m^2) and C_2 is the inertial resistance factor (m^{-1}). For an isotropic polyurethane sponge with porosity ε and mean pore diameter d_p, permeability and inertial resistance are defined using the Ergun relations [30, 33]:

$$K = \frac{d_p^2 \varepsilon^3}{150(1-\varepsilon)^2}, \quad C_2 = \frac{3.5(1-\varepsilon)}{d_p \varepsilon^3} \quad (27)$$

Local thermal equilibrium is assumed between the solid sponge matrix and the saturating fluid. The energy equation inside the porous zone uses an effective thermal conductivity (k_{eff}) [30, 32]:

$$k_{\mathrm{eff}} = \varepsilon k_f + (1-\varepsilon) k_s \quad (28)$$

where k_f and k_s are the thermal conductivities of the fluid and solid sponge material, respectively. Vapour transport in the enclosure is resolved using the Species Transport model (H_2O vapor–air mixture), where the interface saturation vapor pressure and mass fraction are governed by the local interface temperature field (Eqs. 20–24). The thermophysical and structural properties of the porous sponge used in the simulations are: porosity $\varepsilon = [\,0.85]$, permeability $K = [\,1.2 \times 10^{-8}\ \mathrm{m^2}]$, density $\rho_s = [30\ \mathrm{kg/m^3}]$, thermal conductivity $k_s = [0.04\ \mathrm{W/m \cdot K}]$, and specific heat capacity $C_{p,s} = [\,1800\ \mathrm{J/kg \cdot K}]$.

3.4. Developed DSSS

Enhancing the productivity and thermal performance of solar stills has received considerable research attention, particularly through the use of hollow fins as a passive method of improvement. This enhances the heat transfer within the basin and, consequently, the evaporation ratio and the overall thermal performance of the solar desalination system. The impact of hollow fins on DSSS performance can be quantified using the following relations. [26]:

$$A_f = N_f \times \left(\pi \times d_f \times H_f\right) \quad (29)$$

Where A_f is the surface area of the fins (m²), N_f is the Number of fins, and H_f is the fin's height (m).

Total effective heat transfer area A_{tf} (m²) can be determined[٢٧ ,٢٦] :

$$A_{tf} = A_f + A_w \quad (30)$$

Where final productivity with fins m_f (kg/h) can be determined [11-12]:

$$m_f = m_{ew} \times \frac{A_{tf}}{A_w} \times \left(1 + \alpha_f\right) \quad (31)$$

Where α_f It is estimated to be an increase in convective heat transfer due to the copper fins (0.23).

The hourly thermal efficiency of fins η_f can be calculated as follows [28]:

$$\eta_f = \frac{m_f \times \mathrm{h_{fg}}}{I \times \tau.\alpha \times A_W \times 3600} \quad (32)$$

3.5. Meshing of the DSSS simulation model

This paper discusses the method of enhancing heat transfer in a two-dimensional enclosure of triangular shape with fins, as shown in Figure ٥. It is assumed that the flow is steady, incompressible, and laminar, and the problem is solved using the finite volume method with appropriate thermal boundary conditions. The domain was discretized using an unstructured triangular mesh with local refinement

around the fin and porosity. The mesh summaries are as follows: Case A mesh consists of 176,643 elements and 329,316 nodes, Case B mesh consists of 198,000 elements and 365,000 nodes, and Case C mesh consists of 185,000 elements and 342,000 nodes. The mesh quality is 0.71, which guarantees high numerical accuracy as seen in Figure 6.

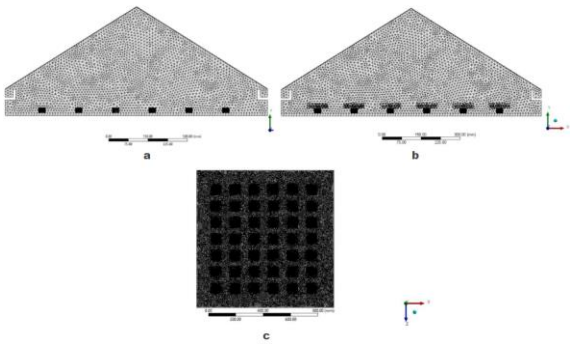


Figure 5. Computational mesh of the investigated DSSS configurations

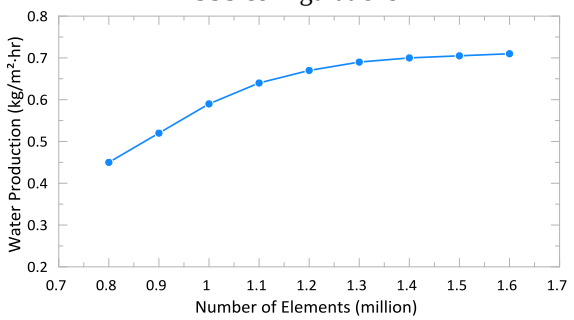


Figure 6. Grid independence test based on water production

3.6 Initial and boundary conditions

ANSYS was used to simulate the DSSS with a single basin, specifying initial and boundary conditions that mimic realistic operating conditions. All the absorber plate, glass and water were equilibrated to ambient temperature (25 °C) at t = 0. The thermal properties of the absorber plate were defined as those of copper in the ANSYS material properties to ensure the hollow fins and the absorber plate are treated as the same material, which allows the maximum possible thermal conductivity. Insulated surfaces were assumed as adiabatic, and the copper absorber plate and the glass cover were assumed to be in contact with convection and radiation with the surrounding:

$$T_w(x,y,z,0) = T_g(x,y,z,0) = T_p(x,y,z,0) = T_a = 25^{\circ}C$$

$$u(x,y,z,0) = 0$$

The surface treated as insulated (back, bottom and lateral surfaces) were treated as ideal minimized surface heat losses. The external glass cover was subjected to radiation and convection heat transfer to simulate environmental heat transfer. In this model, it was assumed that the wind speed would be constant because the external convective heat transfer coefficient is strongly affected by wind speed. Specifically, the external convective heat transfer coefficient between the outer glass cover and ambient environment (h_{ca}) was calculated by the following empirical relation of McAdams [20, 34, 35]: h_{ca}=5.7+3.8V, where V is the average ambient wind speed. This gives a constant external convective heat transfer coefficient to be used along with the external glass emissivity for sky radiation exchange as a mixed thermal boundary condition. The initial heat flux (temperature difference between the heated basin water and the glass surface) results in the internal Grashoff number and condensation rates and is provided by this cooling of the heated basin water by the wind. The system is a closed enclosure, so external ambient humidity was assumed to have a small direct effect on the internal mass transfer and hence was not modelled as one of the key variables. The summary of the conditions at the boundaries is represents in Table 3.

Table 3. Boundary Conditions for Single-Basin DSSS Model

Surface	Boundary Condition
Back side (insulated)	Adiabatic (q = 0)
Bottom side (insulated)	Adiabatic (q = 0)
Lateral sides (insulated)	Adiabatic (q = 0)
Absorber plate	Convection and radiation
Top cover (glass)	Combined external convection and radiation

The finite volume method was used to run the numerical simulations in ANSYS Fluent. To ensure the numbers were correct, a second-order upwind scheme was used to discretize the governing equations for mass, momentum, and energy. The SIMPLE algorithm was used to handle the pressure–velocity coupling. The convergence criteria were set to 10^{-6} for the energy and 10^{-4} for the continuity and momentum equations. The flow within the solar still was assumed to be steady, incompressible, and laminar. The Rayleigh number suggests the flow is laminar. Although a 2D model was used, the dominant heat and mass transfer mechanisms in the system are buoyancy-induced, which can be well-

represented in 2D simulations. This is confirmed by the Rayleigh number which is thought to be in the laminar regime for natural convection in the enclosure. The thermophysical properties of water vapour were assumed to be temperature dependent. We used the surface-to-surface radiation model to accurately represent the heat exchange inside the enclosure. This model includes radiation between the cover and water surface.

4. Validation results

To ensure the accuracy and validity of the present CFD model, a validation process was done by comparing the CFD results with those reported in the literature. The current CFD model was validated by comparing the results with those of Duraid Thamer & Ziyad Tariq[29], who investigated a modified single-slope solar still in a similar climatic zone in Iraq. This involved the yield of fresh water and the basin water temperature. To achieve a solid validation of the present CFD model, the results of the model were validated with reference results of Duraid Thamer & Ziyad Tariq[29] who studied a similar solar still setup. The maximum productivity obtained from the current model was 2.93 kg/m2·day which is different from 2.0 L/m2·day reported in the literature. The difference is quantitatively accounted for by the differences in the basin surface areas as well as the different geographical patterns of solar radiation in the two boundary conditions. The difference in percentage between the predicted hour-wise water temperature of the basin and the reference data is within the tolerance limit of 10%, which is an acceptable limit for a CFD study of solar desalination. Moreover, evaporation trends obtained in Figure 7 corroborate the physical evaporation characteristics reported in the literature, thus validating the use of the used numerical methods, Rayleigh number assumptions and models of radiation between surfaces to correctly simulate the internal heat and mass transfer mechanisms of the solar still. The discrepancy between the results was within the expected range for CFD solar desalination studies. The trends of temperature distribution and productivity augmentation are consistent with other numerical studies, such as Abed et al. [12], and thus validate that the physical models, boundary conditions and numerical methods adopted in this study are suitable for capturing the heat and mass transfer processes in the solar still. Therefore, the present numerical model is well validated and can be used to investigate the impact of hollow fins and porous sponge materials on the performance of the DSSS system.

Table 4. The comparison between previous studies and current work

Study	System Type	Enhancement Technique	Method	Productivity (kg/m²·day)	Improvement (%)
Aftiss et al. [10]	SSSS	PCM integration	Numerical	8.6	—
Abed et al. [12]	Pyramid Still	PCM + Nanoparticles	CFD	8.14	112%
Duraid Thamer & Ziyad Tariq [29]`	DSSS	PCM integration	CFD	1.605	—
Present Work (Case I)	DSSS	Conventional	CFD (ANSYS)	2.93	—
Present Work (Case IV)	DSSS	Hollow fins (49)	CFD	5.03	72%
Present Work (Case V)	DSSS	Fins + porous sponge	CFD	7.88	169%
Present Work (Case VI)	DSSS	Fins + square sponge	CFD	8.79	200% increase compared to Case I

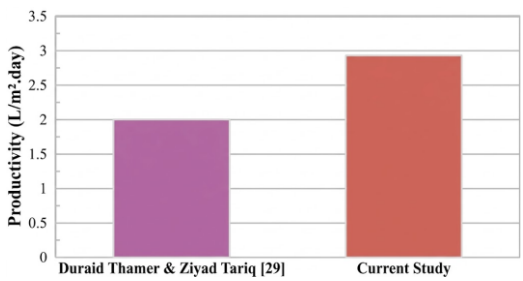


Figure 7. Comparison of freshwater productivity with other study

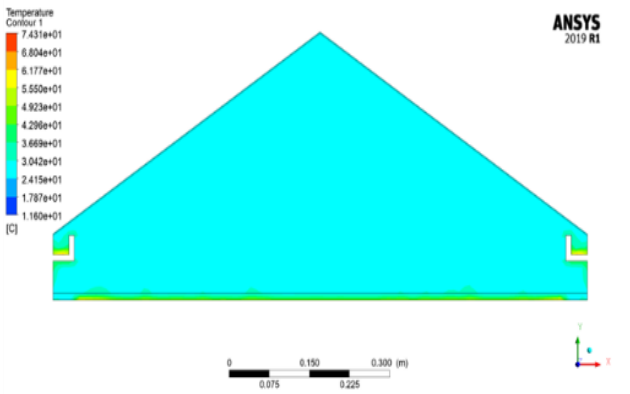
The porous structure facilitates capillary-driven liquid flow, which results in a continuous wetting of the surface and the formation of a thin film. This minimises the interfacial thermal resistance and promotes a vapor diffusion process, resulting in a more uniform vapor distribution and enhanced evaporation. The current study provides one of the highest parameters compared to the literature.

This enhanced performance is due to the combined effect of hollow fins (to increase the heat-transfer area) and the porous sponge materials (to improve the capillary evaporation and water distribution). This approach enhances the evaporation process directly, making the process of producing fresh water more reliable and efficient than PCM-based systems that make use of thermal storage. The heat and mass transfer by the coupled process within the enclosure is responsible for the solar still performance. Hollow fins are used to significantly enhance the heat transfer area that in its turn leads to a rise in the basin temperature and temperature difference. This in turn results in the increase in Grashoff number that in turn is used to reinforce both convection via buoyancy effect and fluid circulation. This ultimately leads to an increase in the convective heat transfer coefficient and therefore, the convective heat transfer rate. At the same time, the porous sponge structure enhances capillary action that helps to achieve even distribution of water and thin film formation on the heat surface. This reduces thermal resistance and provides greater effective evaporation area. The porous structure assists liquid transport through capillarity, ensuring a continuous wetting of the heat surface and thin-film formation. This eliminates thermal contact resistance and promotes vapor diffusion, leading to uniform vapor concentration and enhanced evaporation. This characteristic suggests a shift from thermal- to mass-transfer-limited evaporation, where capillary action-induced thin film dynamics control the evaporation process and hence vapor generation. The enhancement process is determined by thermo-capillary coupling, with increasing temperature difference leading to increasing Grashoff number, which promotes buoyancy-driven convection and increases the convective heat transfer coefficient, thereby resulting in higher evaporative heat flux and higher freshwater production. The freshwater productivity can be determined as a function of evaporative heat flux, and evaporative heat transfer coefficient. Therefore, evaporation and freshwater production are directly proportional to any rise in temperature difference and convective heat transfer coefficient between water and glass. The system behaviour is effectively interpreted using dimensionless parameters.

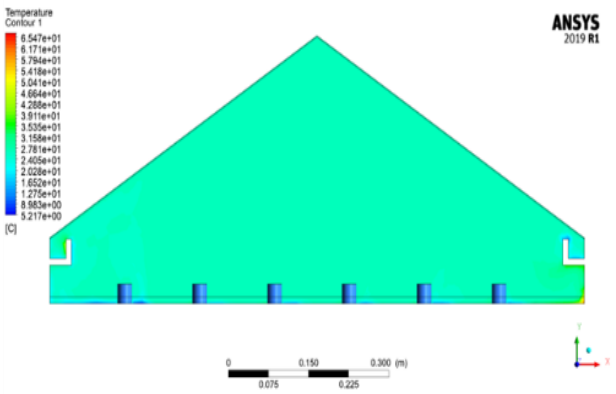
The increase in Grashoff number indicates stronger buoyancy effects and Nusselt Number suggests increased heat transfer by convection. The Rayleigh number was also determined to be $10^4 - 10^6$, thereby validating laminar natural convection in the enclosure.

5. Results and Discussion

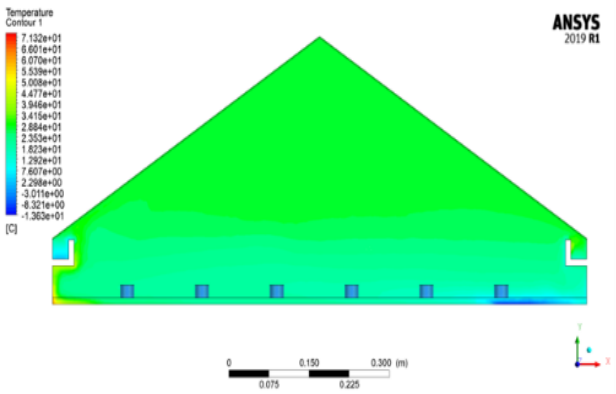
As demonstrated in Figure 8, the temperature distribution indicates that an increase in total effective heat transfer area enhances heat absorption, and consequently, an increase in water temperature results in an increase in temperature difference. This, in turn, leads to an increase in Grashoff number and convective heat transfer coefficient between water and glass, thereby reinforcing natural convection. In Case VI, the porous sponge enhances uniformity by evaporation of thin films, resulting in a more uniform temperature distribution. As illustrated in Figure 9, a plot of velocity contours is presented. With an increase in Grashoff number, buoyancy forces become dominant, resulting in enhanced circulation and improved vapor transport. The porous structure is segmented to minimize stagnant areas and ensure uniform flow. As illustrated in Figures 10 and 11, the distributions of water mass fractions are indicative of the process of evaporation, which is dictated by (evaporative heat transfer coefficient, the difference between saturation vapor pressure at water and glass temperatures). The increase in convective heat transfer coefficient between water and glass results in greater evaporative heat transfer coefficient, and consequently greater evaporative heat flux and mass transfer rate. The diurnal variation of solar radiation used as the main thermal boundary condition for the simulation is shown in Figure 12. This profile is the result of local clear-sky meteorological data from the month of June for Baghdad, Iraq (33.3152N, 44.3661E), the most extreme summertime of the year. As the intensity of the sun increases, so does the evaporative heat flux because of increased heat absorbed, and therefore the productivity of the fresh water increases proportionately. The maximum solar radiation value of 1030 W/m² is adopted to evaluate the system performance under the maximum thermal loading situation in the year, which is referred to peak season.



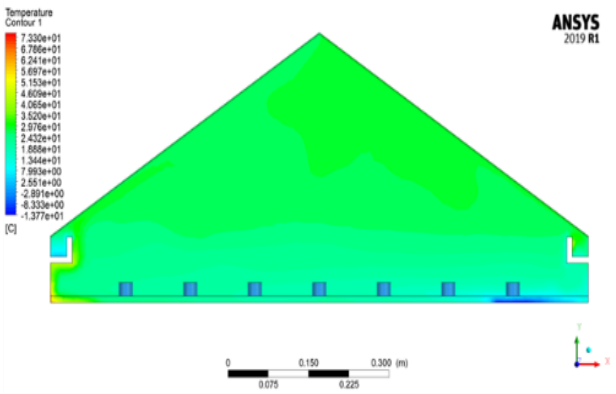
Case I: a DSSS without any modifications



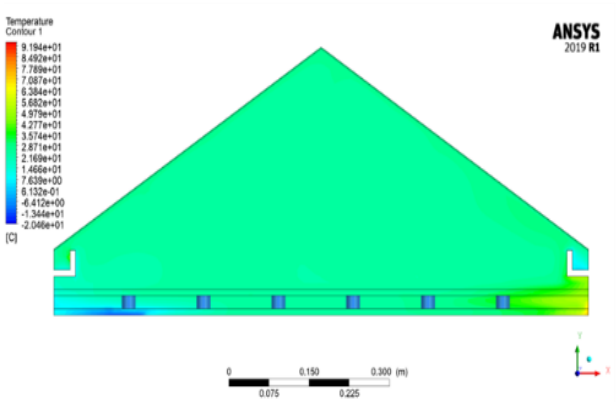
Case II: a DSSS with 36 fins



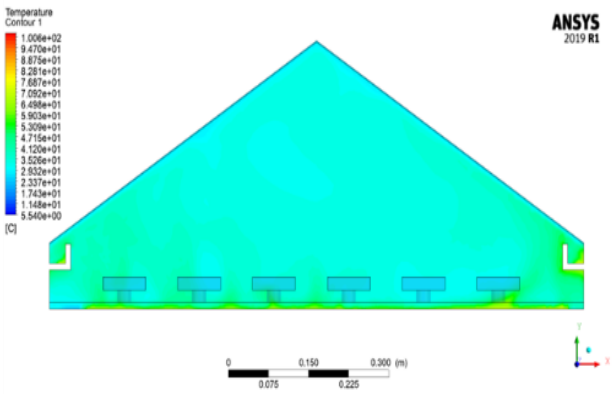
Case III: a DSSS with 42 fins



Case IV: a DSSS with 49 fins



case V: 42 fins with black sponge in a DSSS



case VI: 42 fins with black squar sponges

Figure 8. Temperature contours of the DSSS for different configurations

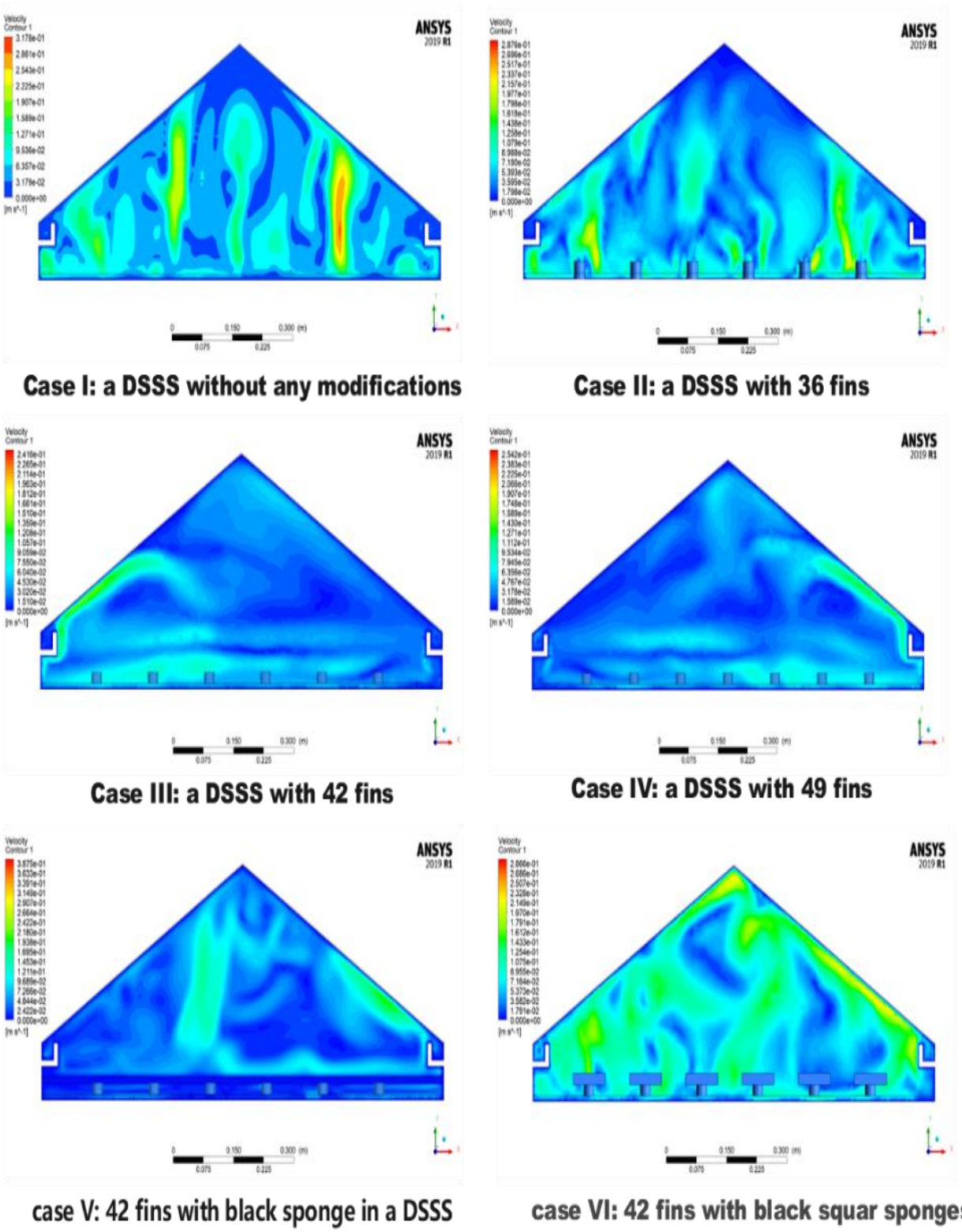


Figure 9. Velocity contours of the DSSS under different configurations

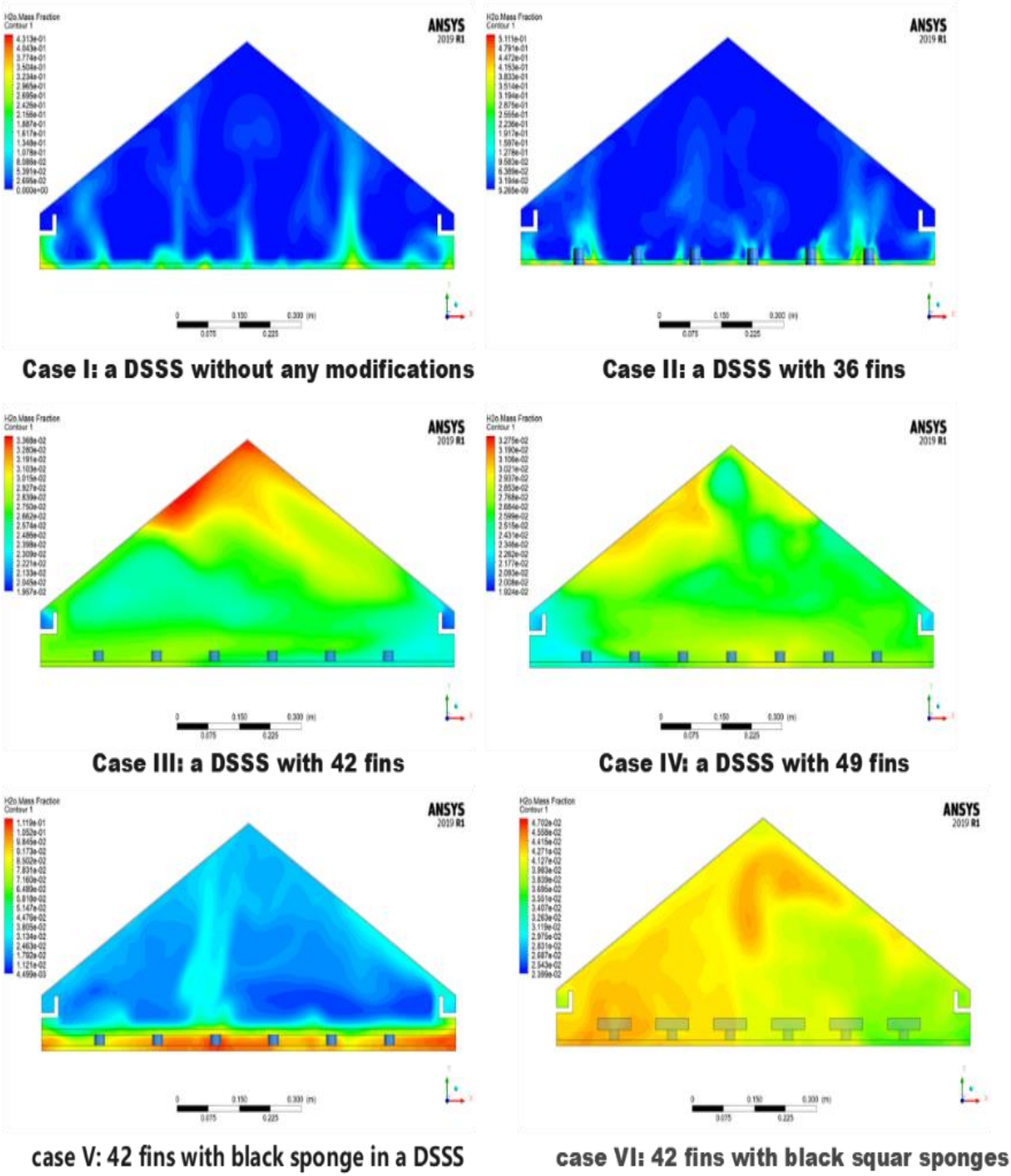


Figure 10. Water mass fraction contours of the DSSS for different configurations

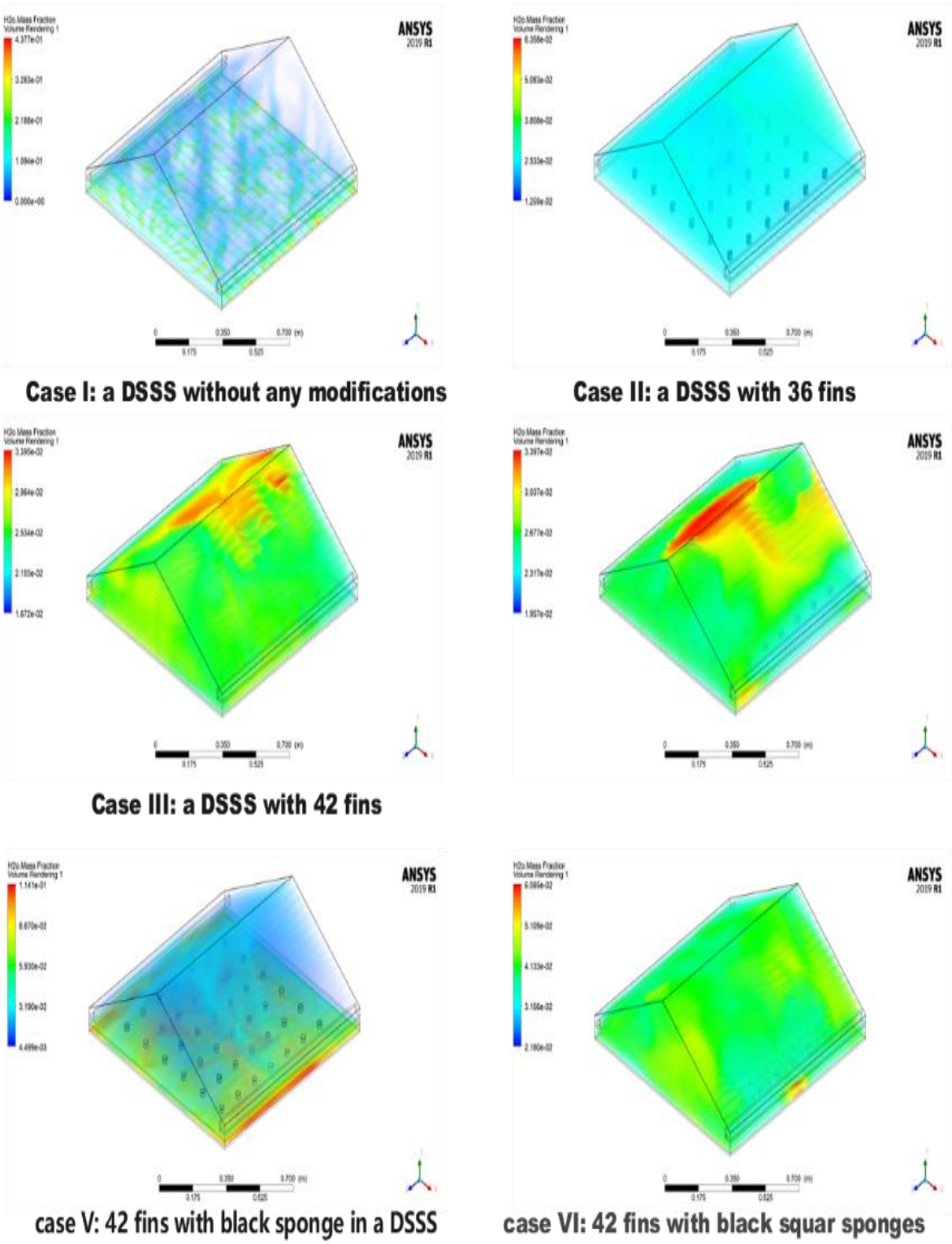


Figure 11. Three-dimensional water mass fraction distribution for different DSSS configurations

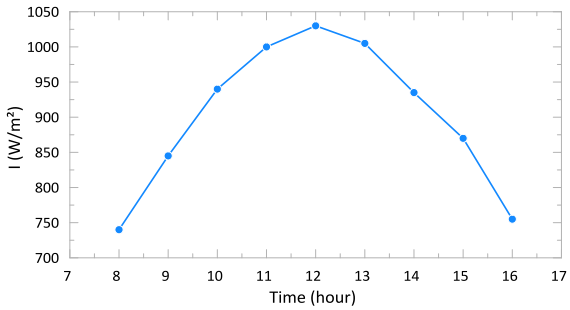


Figure 12. Diurnal Solar Radiation Profile

Figure 13 indicates that the temperature profiles exhibit a normal diurnal cycle, regulated by solar radiation, with the highest temperatures occurring during the day. The standard arrangement is not the most desirable for the lowest temperature, as it has the smallest heat-transfer area, which limits heat absorption and natural convection within the enclosure. The hollow fins increase the effective heat-transfer area, thereby increasing heat absorption and the water temperature in the basin. This will increase the temperature difference between the water in the basin and the glass cover, thereby increasing the Grashoff number and amplifying buoyancy-driven convection within the basin. Further, Cases V and VI are enhanced by adding porous sponge materials that increase the wetted surface area and facilitate thin-film evaporation via capillarity. This allows for even distribution of liquids over the hot surface, minimizes the thermal contact resistance, and facilitates vapor diffusion, thereby enhancing the evaporation process. The segmented porous structure in Case VI also improves performance due to low flow resistance for water distribution and vapor transport. This configuration thus possesses the highest temperature distribution and coupled heat and mass transfer. The effect of the glass cover inclination angle is shown in Figure 14. The traditional solar collectors generally aim to have their inclination angle at an angle equal to the local latitude (about 33° in Baghdad) to ensure that they intercept as much solar radiation as possible; in contrast, a solar still is a complex coupled heat and mass transfer system. A greater inclination angle results in greater sun interception until a critical angle is reached after which it ceases to have any effect, while at the same time providing better gravitational drainage of the condensate.

This effect further raises the temperature difference between the basin water and the glass cover to increase the Grashoff number and hence intensify buoyancy-driven natural convection. The parametric analysis shows that an optimum inclination angle of 32° has been obtained in this geometry Double-Slope Solar Still (DSSS) design. This small latitude exception illustrates that a latitude of 32° is the optimal choice based on thermo-fluid considerations: maximize external solar radiation absorption and optimize the internal natural convection/condensate drainage for maximum freshwater production. To better understand system performance, a sensitivity analysis was performed under various conditions, such as the temperature difference and effective heat transfer area. This shows that small changes in the temperature difference result in substantial changes in the Grashoff number and the convective heat transfer coefficient, implying that system performance is highly sensitive to the thermo-fluid interaction. Figure 15 illustrates the improved productivity with improved heat and mass transfer effects. The productivity of the baseline system is 2.93 kg/m²·day. This productivity can be boosted by adding hollow fins, but the efficiency of a fin density analysis suggests that this will occur with "diminishing returns". The productivities generated in the test beds were 3.87, 4.97 and 5.03 kg/m²·day, respectively for testing arrangements of 36, 42 and 49 fins. The 42-fin configuration was decided to be the best option to maximize efficiency and minimize material and manufacturing costs as it performed near the maximum 49 fin case. For this reason, the best fin arrangement, 42 fins, was chosen for hybrid integration with porous sponge. The maximum productivity was obtained in this combined system (Case VI) with 8.79 kg/m²·day, which is three times that of Case I.. The improvement is due to the collective influence of the effective heat transfer area, the buoyancy-induced convection, and capillary-induced thin-film evaporation, which trigger an enhanced evaporation process and boost vapor transport. As shown in Figure 16, thermal efficiency is proportional to freshwater productivity Eq. (24). Therefore, the increase in freshwater productivity leads to a corresponding improvement in thermal efficiency. The maximum thermal efficiency of Case VI reaches 38.8%, attributed to enhanced coupling between heat and mass transfer processes within the system.

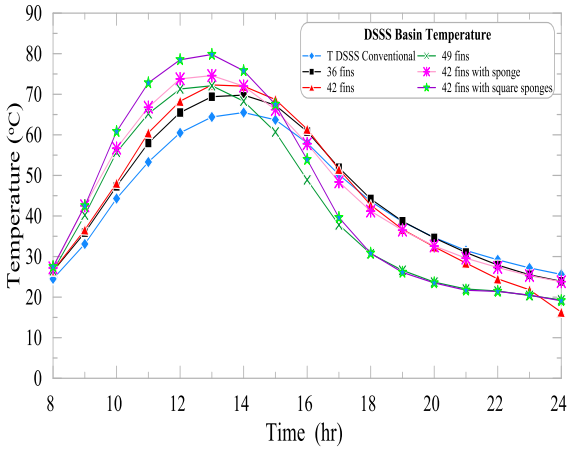


Figure 13. Diurnal variation of basin temperature for different DSSS configurations

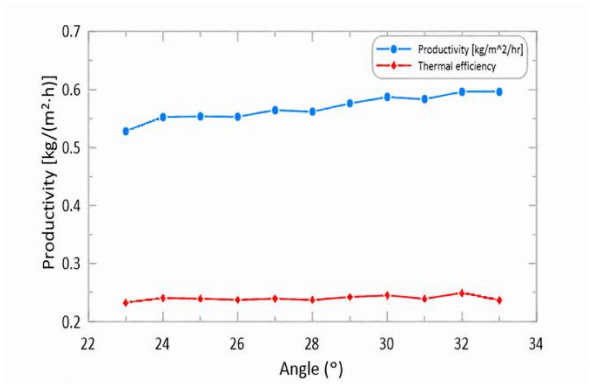


Figure 14. Parametric analysis of glass cover inclination angle on the productivity and thermal efficiency of the DSSS

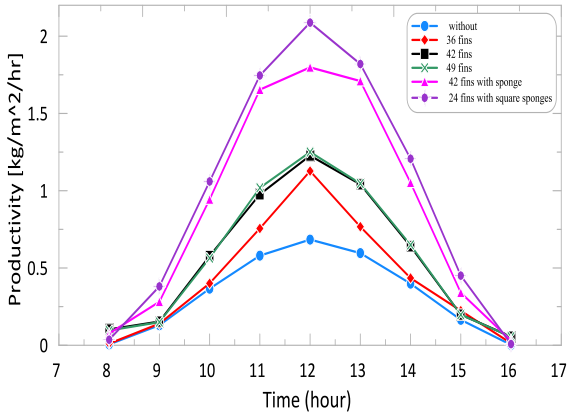


Figure 15. Hourly freshwater productivity for the solar still configurations investigated

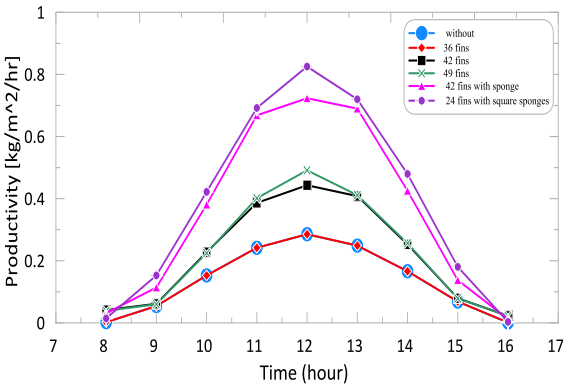


Figure 16. Hourly thermal efficiency of the investigated solar still configurations

6. Conclusion

ANSYS Fluent was employed to perform numerical simulations under the climatic conditions of Baghdad, Iraq (33.3152°N, 44.3661°E). The simulations were conducted under peak solar radiation conditions (June), representing the most critical operating scenario.

1. A parametric investigation (Case I) was conducted to determine the optimal glass cover inclination angle, to find the best angle of cover to be used with the glass covers in the range of 23° to 33°. The best inclination angle for all configurations under study found to be 32°.The conventional DSSS produced a freshwater productivity of 2.93 kg/m²·day with an average thermal efficiency of 13.6%.
2. The effective heat transfer area and evaporation were augmented by adding hollow fins. Freshwater productivity and thermal efficiencies were:
    - Case II 36 fins: 3.87 kg/m²·day, and 13.6%
    - Case III 42 fins: 4.97 kg/m²·day, and 21.4%,
    - Case IV 49 fins: 5.03 kg/m²·day, and 22
    - .1%.
3. The 42-fin configuration was selected for sponge integration because its performance was close to the 49-fin case, while reducing manufacturing cost. The incorporation of porous sponge materials enhanced evaporation through capillary-driven thin-film mechanisms as the following:

- Case V: The continuous sponge layer produced 7.88 kg/m²·day at 35.4% efficiency.
- Case VI: The square sponge configuration achieved the best performance, 8.79 kg/m²·day at 38.8% efficiency, an approximately threefold increase over Case I.

4. The present numerical investigation yields promising results but has some restrictions. The 2D CFD model is a well valid model for predicting the internal heat and mass transfer behaviours, which is, however, ideal and continuous operating conditions are assumed for the model. It doesn't include any possible edge effects on the boundary that is 3D, nor does it consider any long-term degradation of the physical properties of the system such as salt scaling or biological fouling of the porous sponge structure. Thus, it is recommended that a physical prototype be fabricated and tested in the future for the optimized 42-fin and segmented square sponge configuration. To prove the accuracy of the numerical predictions in dynamically changing real-world meteorological conditions for long-term periods, experimental studies are needed. In addition, in-depth thermo-economic and exergy analysis is advised to achieve the accurate assessment of long-term cost effectiveness, maintenance needs and commercial feasibility of this hybrid solar desalination system.

Nomenclature

2D	Two-Dimensional
3D	Three-Dimensional
ANSYS	Engineering simulation software used for numerical analysis
CFD	Computational Fluid Dynamics
DSSS	Double-Slope Solar Still
H_2O	Water vapor/water
PCM	Phase Change Material
PSS	Pyramid Solar Still
SSSS	Single-Slope Solar Still

Symbol	Meaning	Unit
Af	Fin surface area	m²
g	Gravitational acceleration	m/s²
Gr	Grashof number	—
h_{Cw}	Convective heat transfer coefficient between water and glass	W/m²·°C
$h_{cw,CL}$	Convective heat transfer coefficient based on the Clark model	W/m²·°C
$h_{cw,D}$	Convective heat transfer coefficient based on the Dunkle model	W/m²·°C
$h_{cw,KT}$	Convective heat transfer coefficient based on the Kumar and Tiwari model	W/m²·°C
h_{ew}	Evaporative heat transfer coefficient	W/m²·°C
h_{ewD}	*Evaporative heat transfer coefficient based on the Dunkle model*	*W/m²·°C*
H_f	*Fin height*	*m*
A_f	*Fin surface area*	*m²*
A_{tf}	*Total effective heat transfer area*	*m²*
A_W	*Water surface area*	*m²*
C	*Empirical constant*	—
Cp	*Specific heat at constant pressure*	*J/kg·K*
Cv	*Specific heat capacity of water vapor*	*J/kg·°C*

References

1. UNESCO World Water Assessment Programme, *The United Nations World Water Development Report 2021: Valuing Water*. UNESCO, Paris, 2021. https://doi.org/10.54679/MOMU6572.
2. Alkaisi, A., Mossad, R., and Sharifian-Barforoush, A., A review of the water

desalination systems integrated with renewable energy. *Energy Procedia*, 2017, **110**, 268–274. https://doi.org/10.1016/j.egypro.2017.03.138.

3. Toulan, Y.A., et al., Numerical study of productivity enhancement of solar still using different absorber designs. *Applied Thermal Engineering*, 2025, **275**, 126786. https://doi.org/10.1016/j.applthermaleng.2025.126786.
4. Ghazy, A., Theoretical study of a double-slope solar still with solar air heater condenser. *International Journal of Renewable Energy Development*, 2023, **12**(6), 977–986. https://doi.org/10.14710/ijred.2023.53928.
5. Rajaseenivasan, T. and Srithar, K., Performance investigation on solar still with circular and square fins in basin with CO2 mitigation and economic analysis. *Desalination*, 2016, **380**, 66–74. https://doi.org/10.1016/j.desal.2015.11.025.
6. Khare, V.R., et al., Modelling and performance enhancement of single slope solar still using CFD. *Energy Procedia*, 2017, **109**, 447–455. https://doi.org/10.1016/j.egypro.2017.03.064.
7. Moreno, S., Álvarez, C., Hinojosa, J.F., and Maytorena, V.M., Numerical analysis of a solar still with phase change material under the basin. *Journal of Energy Storage*, 2022, **55**, 105427. https://doi.org/10.1016/j.est.2022.105427.
8. Hafs, H., Ansari, O., and Bah, A., Performance evaluation of a production system of solar desalination by using rectangular channels with PCM at different seasons. *Acta Ecologica Sinica*, 2023, **43**(4), 690–700. https://doi.org/10.1016/j.chnaes.2022.09.001.
9. Hameed, H.G., Diabil, H.A.N., and Al-Moussawi, M.A., A numerical investigation of the enhancement of single-slope single-basin solar still productivity. *Energy Reports*, 2023, **9**, 484–500. https://doi.org/10.1016/j.egyr.2022.11.199.
10. Aftiss, R., Najim, M., and Hissouf, M., Numerical study of PCM-integrated solar still efficiency enhancement. *International Journal of Low-Carbon Technologies*, 2024, **19**, 443–454. https://doi.org/10.1093/ijlct/ctae004.
11. AbdelMeguid, H. and El Awady, W.M., Optimizing solar still performance through glass cover optical properties: A mathematical modeling and theoretical investigation. *Ain Shams Engineering Journal*, 2024, **15**(3), 102589. https://doi.org/10.1016/j.asej.2023.102589.
12. Abed, A.F., Alshukri, M.J., and Hachim, D.M., Improving solar still performance via the integration of nanoparticle-enhanced phase change materials: A novel pyramid-shaped design with a numerical simulation approach. *Journal of Energy Storage*, 2024, **97**, 112980. https://doi.org/10.1016/j.est.2024.112980.
13. Aftiss, R., Najim, M., Tbatou, T., and Hissouf, M., Numerical study of conventional solar still integrated dynamic PCM layer. *Desalination*, 2025, **600**, 118493. https://doi.org/10.1016/j.desal.2024.118493.
14. Togun, H., Homod, R.Z., Sadeghinezhad, E., and Kazi, S.N., Navier-Stokes equations and high-resolutions: Advancements in accurate incompressible flow simulations. *Knowledge-Based Engineering and Sciences*, 2023, **4**(2), 51–59. https://doi.org/10.51526/kbes.2023.4.2.51-59.
15. da Silva Junior, L.G., de Oliveira, J.P.J., Ribeiro, G.B., and Ferreira Pinto, L., Experimental and numerical analysis of a low-cost solar still. *Eng*, 2023, **4**(1), 380–403. https://doi.org/10.3390/eng4010023.
16. Gaur, M.K. and Tiwari, G.N., Optimization of number of collectors for integrated PV/T hybrid active solar still. *Applied Energy*, 2010, **87**(5), 1763–1772. https://doi.org/10.1016/j.apenergy.2009.10.019.
17. Kumar, S. and Tiwari, G.N., Estimation of convective mass transfer in solar distillation systems. *Solar Energy*, **1996**, **57**(6), 459–464. https://doi.org/10.1016/S0038-092X(96)00122-3.
18. Al-Sulttani, A.O., et al., Double-slope solar still productivity based on the number of rubber scraper motions. *Energies*, 2022, **15**(21), 7881. https://doi.org/10.3390/en15217881.
19. Suneesh, P.U., Jayaprakash, R., Namshad, T., and Kumar, S., Performance of corrugated wick in "V" type solar still. *Smart Grid and*

Renewable Energy, 2013, **4**(8), 483–487. https://doi.org/10.4236/sgre.2013.48055.

20. Elango, C., Gunasekaran, N., and Sampathkumar, K., Thermal models of solar still—A comprehensive review. *Renewable and Sustainable Energy Reviews*, 2015, **47**, 856–911. https://doi.org/10.1016/j.rser.2015.03.054.
21. Tiwari, G.N., Shukla, S.K., and Singh, I.P., Computer modeling of passive/active solar stills by using inner glass temperature. *Desalination*, 2003, **154**(2), 171–185. https://doi.org/10.1016/S0011-9164(03)80018-8.
22. Abderachid, T. and Abdenacer, K., Effect of orientation on the performance of a symmetric solar still with a double effect solar still (comparison study). *Desalination*, 2013, **329**, 68–77. https://doi.org/10.1016/j.desal.2013.09.011.
23. Ghazy, A. and Alrowais, R., Experimental performance of single-slope basin solar still coupled with a humidification–dehumidification cycle. *Sustainability*, 2022, **14**(23), 15755. https://doi.org/10.3390/su142315755.
24. Suraparaju, S.K., et al., Innovative double-finned absorber and nanoparticle-enhanced energy storage for enhanced thermo-economic performance of solar stills. *Separation and Purification Technology*, 2025, **361**, 131360. https://doi.org/10.1016/j.seppur.2024.131360.
25. Rahman, T., Enhancing solar still performance using external condensers and floating fins: A comparative study. *Cleaner Chemical Engineering*, 2025, **11**, 100167. https://doi.org/10.1016/j.clce.2025.100167.
26. Abdelgaied, M., et al., Improving the tubular solar still performance using square and circular hollow fins with phase change materials. *Journal of Energy Storage*, 2021, **38**, 102564. https://doi.org/10.1016/j.est.2021.102564.
27. Mohammed, S.A., et al., Pyramidal solar stills via hollow cylindrical perforated fins, inclined rectangular perforated fins, and nanocomposites: An experimental investigation. *Sustainability*, 2022, **14**(21), 14116. https://doi.org/10.3390/su142114116.
28. El-Sebaii, A.A., Ramadan, M.R.I., Aboul-Enein, S., and El-Naggar, M., Effect of fin configuration parameters on single basin solar still performance. *Desalination*, 2015, **365**, 15–24. https://doi.org/10.1016/j.desal.2015.02.002.
29. Mahmood, D.T. and Sfaieeh, Z.T., Enhancing the performance of a double-slope solar still using thin and twisted fins: A numerical study. *Journal of Solar Energy Research*, 2026, **11**(3), 3221–3235. https://doi.org/10.22059/jser.2026.415805.1759.
30. ANSYS Inc., *ANSYS Fluent Theory Guide, Release 19.1*. ANSYS Inc., Canonsburg, PA, 2018.
31. Rashidi, S., Bovand, M., Rahbar, N., and Esfahani, J.A., Steps to improve the performance of a solar still by installing a porous medium: A numerical and experimental study. *Renewable Energy*, 2018, **115**, 769–780. https://doi.org/10.1016/j.renene.2017.08.095.
32. Nield, D.A. and Bejan, A., *Convection in Porous Media*, 5th ed. Springer, Cham, 2017. https://doi.org/10.1007/978-3-319-49562-0.
33. Ergun, S., Fluid flow through packed columns. *Chemical Engineering Progress*, 1952, **48**(2), 89–94.
34. McAdams, W.H., *Heat Transmission*, 3rd ed. McGraw-Hill, New York, 1954.
35. Duffie, J.A. and Beckman, W.A., *Solar Engineering of Thermal Processes*, 4th ed. John Wiley & Sons, Hoboken, NJ, 2013. https://doi.org/10.1002/9781118671603.